Catalysis Science & Technology

ROYAL SOCIETY OF CHEMISTRY

PAPER

View Article Online
View Journal | View Issue

Cite this: *Catal. Sci. Technol.*, 2020, 10, 3938

Organometallic chemical deposition of crystalline iridium oxide nanoparticles on antimony-doped tin oxide support with high-performance for the oxygen evolution reaction†

Ziba S. H. S. Rajan, [a] Tobias Binninger, [b] Patricia J. Kooyman, [c] Darija Susac [a] and Rhiyaad Mohamed *[a]

Received 9th March 2020,
Accepted 26th May 2020

DOI: 10.1039/d0cy00470g

rsc.li/catalysis

The design of efficient, robust catalytic materials for the anodic evolution of oxygen in proton exchange membrane water electrolysers remains a great challenge to be overcome for the commercialisation of this promising hydrogen generating technology. In the present work, we demonstrate a simple, one-step organometallic chemical deposition (OMCD) of IrO_2 nanoparticles onto Sb-doped SnO_2 (ATO) high-surface area support. The resulting IrO_2/ATO electrocatalyst was characterised using high-resolution scanning transmission electron microscopy (HR-STEM) and X-ray photoelectron spectroscopy (XPS) to develop an understanding towards the structural and chemical properties of the prepared materials. The OMCD method produced crystalline IrO_2 nanoparticles of 2.3 ± 0.7 nm that were uniformly dispersed over the ATO support surface. Most interestingly, structural metal–support interactions were observed in the form of epitaxial anchoring of IrO_2 nanoparticles on the ATO support. These characteristics yielded outstanding oxygen evolution performance: a 7-fold increase in Ir mass-specific activity was observed compared to an IrO_2–TiO_2 commercial benchmark, in combination with excellent stability of our crystalline IrO_2.

1. Introduction

The generation of high purity hydrogen by renewable, sustainable means is a crucial building block towards the realisation of a carbon-free energy economy. Proton exchange membrane (PEM) water electrolysis offers a promising route for the generation of clean hydrogen, using renewable energy, for both stationary and mobile energy storage applications and as a feedstock for the chemical industry. As water electrolysis is an electrochemical redox reaction, cathodic hydrogen evolution cannot occur without an efficient and rapid anodic oxygen evolution reaction (OER). While both iridium and ruthenium oxides are state-of-the-art OER catalysts in acidic environment, the latter undergoes dissolution under anodic OER conditions much more rapidly than the former, and this makes iridium oxide the most suitable catalytic material for PEM water electrolyser anodes.[1]

For electrolyser technology to reach widespread commercialisation, it is critical that the iridium loading in anode catalysts is reduced to a point where the performance of these catalysts greatly outweighs their cost. Various approaches have been explored to lower iridium content while maintaining high OER performance: iridium–iridium oxide core–shell concepts,[2,3] bimetallic oxides,[4,5] high-surface area amorphous iridium oxides,[6,7] and the use of iridium oxide nanoparticles supported on inexpensive materials[8–20] to enhance iridium utilisation by maximising the electrocatalytically active surface area.

For the latter approach, the support materials need to exhibit high surface area and be electronically conductive as well as low cost materials, which are capable of forming porous structures that are stable in highly acidic and oxidising environments. These are challenging criteria to meet, and while carbon has played a starring role as an electrocatalytic support material in fuel cell applications, it is unsuitable for anodic electrolyser applications as a result of carbon corrosion which is prominent at the high oxidative potentials ($E > 1.5$ V *vs.* the reversible hydrogen electrode (RHE)) of the oxygen evolution reaction.[21,22]

Sasaki *et al.*[23] evaluated the thermodynamic stability of various metal oxides as alternative support materials to

[a] *HySA/Catalysis Centre of Competence, Catalysis Institute, Department of Chemical Engineering, University of Cape Town, 7701, South Africa. E-mail: rhiyaad.mohamed@uct.ac.za*
[b] *IBM Research – Zurich, Säumerstrasse 4, Rüschlikon CH-8803, Switzerland*
[c] *Centre for Catalysis Research, Catalysis Institute, Department of Chemical Engineering, University of Cape Town, 7701, South Africa*

† Electronic supplementary information (ESI) available. See DOI: 10.1039/d0cy00470g

carbon black, under severe operating conditions for PEM fuel cell applications. Thermodynamic calculations showed that SnO_2 and TiO_2 are feasible, oxidation-resistant support materials, particularly in instances where the operating potential exceeds 1.4 V *vs.* RHE. While this is a strong motivation for the use of such materials as electrolyser supports, these oxides offer little electronic conductivity. Doping with metal cations or anions such as fluoride can create electronic defects in these materials, and subsequently create the desired electronic conductivity.[24–26] Over the past five years, antimony-doped tin oxide (ATO) has gained significant attention as an anodic catalyst support material for Ir-based catalysts in OER applications. ATO-supported iridium-based electrocatalysts have proven themselves to be highly effective OER catalysts; they can exhibit high OER mass-specific activity, while simultaneously utilising much less iridium than is required for unsupported iridium-based OER catalysts. Nanoparticles of various iridium phases (Ir metal, partially-oxidised oxyhydroxides (IrO_x), and iridium oxide with the rutile structure (IrO_2)) have been deposited onto ATO support by means of Adams' fusion,[14,20] a colloidal method,[19] hydrothermal synthesis,[27] chemical reduction as a means to deposit IrO_x nanoparticles on ATO aerogels,[18,28] and a solvothermal technique for the deposition of IrO_2 on macroporous ATO support. Some of these wet synthesis methods combine the ATO support with independently synthesised IrO_x particles,[11,15,16] and this can cause a superficial attachment between the catalyst and support. In other studies, metallic Ir nanodendrites or nanoparticles were deposited on ATO support by means of chemical reduction,[15] the polyol method,[16,28,29] and microwave-assisted hydrothermal deposition.[10] While these methods have been successful, they often require numerous steps, typically including a calcination step to strengthen the bond between the catalyst and ATO support. While calcination is necessary, it tends to cause particle agglomeration.

An organometallic chemical deposition (OMCD) method was found to be highly successful in the deposition of Pt nanoparticles on carbon, carbide and oxide support materials[30–32] with a narrow size range and high spatial dispersion. As ATO has been shown to interact with IrO_x in a manner that improves the overall OER performance of supported IrO_x/ATO catalysts,[16,33] the fact that the OMCD method is a purely thermal deposition process suggests that the use of such a method could result in superior fortification of the IrO_2–ATO interface, while simultaneously avoiding the unnecessary migration of nucleated particles, resulting in OER performance which surpasses the performance of similar materials prepared by traditional wet synthesis methods. In addition, OMCD is a one-step method that offers simplicity in comparison to wet chemistry techniques which contain numerous process and post-treatment steps.

In the present work, we investigate the viability of OMCD for the deposition of iridium oxide nanoparticles on ATO support. The *ex situ* OER performance of this electrocatalyst was evaluated using the rotating disk electrode (RDE) technique. The structural and chemical characteristics of the iridium oxide were studied using high-resolution scanning transmission electron microscopy (HR-STEM) and X-ray photoelectron spectroscopy (XPS), in order to understand the observed oxygen evolution activity and stability of OMCD IrO_2/ATO.

2. Experimental

2.1 Deposition of iridium oxide nanoparticles onto ATO support

ATO nanopowder (99.95+% pure, approx. 30 nm particle size, $SnO_2:Sb_2O_3$ = 90 : 10 wt%, 95 $m^2\ g^{-1}$, 0.02 S cm^{-1}, obtained from US Research Nanomaterials Inc.) was used as the support material. Fig. S1 in the ESI† shows the X-ray diffractogram of the ATO nanopowder. Iridium tris-acetylacetonate, $Ir(acac)_3$ (97% pure from Sigma-Aldrich), was used as the organometallic precursor for the iridium oxide deposition process. To confirm reproducibility of the process, we prepared and characterised two independent batches of the electrocatalyst. All synthesised catalysts were prepared using OMCD: 200 mg of ATO powder was thoroughly mixed with 132 mg of $Ir(acac)_3$ powder (to obtain a nominal loading of 20 wt% Ir) and crushed using a mortar and pestle. The solid powder mixture was placed inside a 20 mL stainless steel reactor vessel and this reactor was then inserted into a tubular furnace. The first and second stages of the process involve the removal of water from the ATO + $Ir(acac)_3$ mixture by heating the reactor vessel to 100 °C and holding at this temperature for half an hour; during this process the reaction gas, pure oxygen, was flowed through the reactor tube at 20 mL min^{-1} to flush the reaction volume. The reaction chamber was then sealed, enclosing oxygen gas and the dry ATO + $Ir(acac)_3$ mixture. The vessel was heated to 320 °C and held at this temperature for a period of 2 h, after which it was allowed to cool down to room temperature before collection of the IrO_2/ATO electrocatalyst powder. A schematic representation of the deposition process is shown in Fig. 1(a) and the temperature profile of the various steps in the deposition process is shown in Fig. 1(b).

2.2 Physical characterisation

One of the challenges faced in this work was in the reliable determination of the Ir mass-content in the IrO_2/ATO catalysts. As the samples could not be digested completely in *aqua regia* (not even with the addition of hydrofluoric acid), inductively coupled plasma optical emission spectroscopy (ICP-OES) could not be used as a meaningful quantification technique. Energy dispersive X-ray spectroscopy (EDX) was therefore applied to quantify the mass of iridium present in the electrocatalysts.

A scanning electron microscope (SEM), FEI Nova Nano SEM 230 with a field emission gun (FEG), was used to collect energy dispersive X-ray spectra at 20 kV using an Oxford X-Max detector and INCA software. An IrO_2–TiO_2 commercial

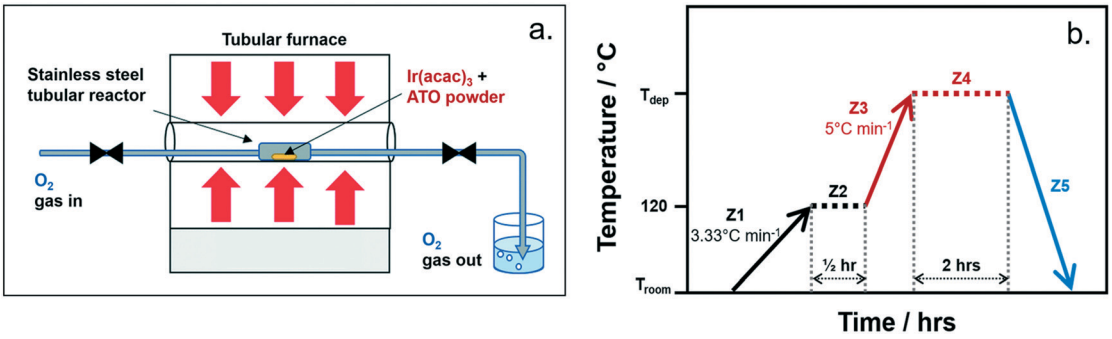

Fig. 1 (a) Diagram illustrating the OMCD catalyst preparation process, adapted from Mohamed *et al.*,[32] (b) temperature profile for the OMCD process where Z1 and Z2 involve the removal of water from the ATO/Ir(acac)$_3$ mixture by heating the reactor vessel to 100 °C and holding at this temperature for half an hour, Z3 is heating to the desired deposition temperature, and Z4 is held here for a period of 2 hours, after which the reactor is allowed to cool down to room temperature (Z5) before collection of the IrO_2/ATO catalyst powder.

catalyst (Elyst Ir75, Umicore AG & Co. KG), with a known iridium mass content of 74.4 wt% (as given in the batch specifications), was analysed using EDX; a result of 71.8 ± 1.9 wt% of iridium was obtained, validating the suitability of this technique to quantify the mass of iridium present in the IrO_2/ATO catalysts. To increase the precision of the measurement, a series of standards was prepared (ranging from 10 to 50 wt% Ir) by diluting the commercial IrO_2–TiO_2 catalyst with titania and the resulting calibration plot (Fig. S2 in ESI†) was used to determine the iridium mass loading of OMCD IrO_2/ATO from EDX spectra.

Structural characterisation was performed using a Bruker D8 Advance X-ray diffractometer operating at 40 kV with a Co-K_α radiation source, and a JEOL JEM ARM200F double Cs-corrected high-resolution scanning transmission electron microscopy (HR-STEM) equipped with a field emission gun (FEG) and a high angle annular dark field (HAADF) detector, operated at 200 kV. An Oxford XMax 100 TLE EDX detector was used for elemental mapping to gain a qualitative understanding of the iridium dispersion. Image J software was used as a counting tool to quantify the particle sizes of the IrO_2 nanoparticles. 330 particles were counted and it was ensured that the Feret diameter, the maximum length across a non-spherical particle, was measured for particle size. Normalisation of the histogram was done with respect to the number of particles counted. The *d*-spacings within IrO_2 particles were extracted from lattice fringes visible in HR-STEM images, using the plot profile function in Image J.

X-ray photoelectron spectroscopy (XPS) was used to gain an understanding of the iridium oxidation phases present in IrO_2/ATO. A PHOIBOS 150 electron analyser (SPECS GmbH) with a monochromated Al K_α source (1486.71 eV) was used. The energy resolution was set to 0.7 eV for survey spectra and 0.5 eV for all other spectra. The charging of the sample surface was compensated by application of a low-energy electron flood gun where the electron energy was 2 eV, and the electron flux was 20 μA.

Ir 4f and O 1s components were fit using XPSPeak4.1 software, applying an approach that is in agreement with previously published work by Pfeifer *et al.*[34] and Yu *et al.*[35] A Lorentzian/Gaussian ratio of 20 was used for all Ir 4f components. A full width at half maximum (FWHM) of 1.2 eV was used for Ir^{4+} and Ir^{3+}, 2.4 eV for the satellite peaks occurring at 62.8 eV and 63.3 eV, and 1.7 eV for the satellite peak at 67.8 eV. All photoelectron peaks were fit using an asymmetric Gaussian–Lorentzian sum peak function and peak tail asymmetry factors of 0.2 and 100 were applied for Ir 4f, TS and TL.

For the O 1s spectrum, first, the contribution from an overlapping component Sb $3d_{5/2}$ was determined using the area measurement under Sb $3d_{3/2}$ at 540.4 eV, and taking into account the area ratios between Sb $3d_{5/2}$ and $3d_{3/2}$. All oxygen components were then fit with a FWHM of 1.5 eV and Lorentzian/Gaussian ratio of 20. Asymmetry factors TS 0.1 and TL 100 were applied for Sb $3d_{5/2}$, as well as for oxygen bound to metallic components.

2.3 Working electrode preparation

Porous thin-film electrodes were prepared from ink dispersions that were drop-cast onto 0.196 cm^2 glassy carbon electrode disks. The inks consisted of 1.00 ml of water, 4.00 ml of ethanol, 20 μl of Nafion® ionomer solution (5 wt% in water and aliphatic alcohols, Fuel Cell Earth), and 10 mg of the IrO_2/ATO or IrO_2–TiO_2 commercial benchmark catalyst to be tested. OMCD IrO_2/ATO and IrO_2–TiO_2 electrodes were prepared to have a catalyst electrode loading of 400 μg cm^{-2} and 100 μg cm^{-2}, respectively. These loadings were selected in order to compare OER electrochemical experiments for similar iridium mass present on the rotating disk electrode (RDE). Furthermore, for IrO_2–TiO_2, an electrode catalyst loading of 100 μg cm^{-2} is most commonly used in the literature, thus measuring its OER *ex situ* performance at this loading provided us with means to validate the electrochemical testing methods and apparatus used in our work. However, as electrode loading/thickness is known to affect RDE results,[10] IrO_2–TiO_2 was also studied using electrodes prepared with the same electrode catalyst loading of 400 μg cm^{-2} (see Fig. S3(b) in ESI†). The catalyst inks were ultra-sonicated for 30 min before deposition. To ensure that

the ink deposited on the electrodes was always well-dispersed, the ink was undergoing magnetic stirring during the filling of a micropipette. A quantity of 40 μl of catalyst ink was deposited onto each glassy carbon disk to attain an electrode loading of 400 μg cm^{-2}, whereas 10 μl was deposited to achieve 100 μg cm^{-2}. All electrodes were dried at room temperature in air.

2.4 Electrochemical characterisation

Electrochemical characterisation was performed using a RDE set-up (150 mL glass cell, Pine Research Instrumentation) and 100 mL of 0.1 M perchloric acid electrolyte (prepared from 60% stock solution from Kanto Chemical Company). A Hg/Hg_2SO_4 reference electrode, with a calibrated potential of 0.720 V *vs.* RHE, a platinum wire counter electrode, and the catalyst thin-film working electrode were used in a three-electrode cell set-up. Three working electrodes were prepared and characterised for each OMCD catalyst batch to study the reproducibility of the synthesis, as well as to estimate the error of the results. All potentials are reported *versus* RHE.

Several O_2 bubbles evolve at high potentials (1.600 V *vs.* RHE onwards), which can block active electrochemical reaction sites. Rotation is beneficial for the removal of evolved bubbles to retain the accuracy of the measurement;[36] the working electrode was therefore rotated at 1600 rpm. To further improve the bubble removal, which was particularly important for the stability portion of the testing protocol, the RDE set-up was tilted at an angle between 15 and 30°.

All electrodes were subjected to cyclic voltammetry (CV) at the beginning of the electrochemical protocol to clean and activate the catalyst layer. For this purpose, 10 potential cycles were carried out from 1.000–1.400 V *vs.* RHE at 50 mV s^{-1} (see Fig. S3(a) in ESI†), followed by a further 10 cycles in the same potential range, at 10 mV s^{-1}. Thereafter, the catalyst was subjected to successive activation steps using chronoamperometry from 1.400–1.480 V *vs.* RHE in 20 mV steps, for a duration of 1 minute per step. Chronoamperometry was also utilised for measuring OER activity and stability: the potential was stepped up from 1.500–1.560 V *vs.* RHE, holding for 1 minute per step. To remove the effect of transient capacitive currents, only the last 30 seconds of each step were used for OER activity analysis, because the currents in this portion of the measurement are assumed to be controlled predominantly by the OER reaction kinetics.[37] Electrochemical impedance spectroscopy (EIS) was performed at 1.000 V *vs.* RHE in the frequency range from 200 kHz to 100 mHz, to determine the effective ohmic resistance used for iR-correction. For technically relevant comparability of the results, the OER currents were converted to Ir mass-specific activity by normalisation with respect to the mass of iridium present on the RDE. The latter was calculated from the iridium mass percentage in the catalyst determined by EDX as described previously. A commercial IrO_2–TiO_2 OER catalyst (Elyst Ir75, Umicore AG & Co. KG) was used as a benchmark to gauge the performance of our catalyst in comparison to a state-of-the-art commercially available catalyst.

The stability of the electrocatalysts was evaluated by applying a potential of 1.600 V *vs.* RHE for a period of 2 hours, after which the catalyst was again subjected to the OER activity protocol (described above) to determine the relative loss of mass-specific activity. Potentials exceeding 1.600 V *vs.* RHE were not explored for stability measurements: at these potentials, the OER reaction rate was so high that large numbers of O_2 bubbles were produced within the porous catalyst layer, causing blocking and detachment of the catalyst from the glassy carbon electrode.

Normalisation of the current responses obtained in all the electrochemical experiments performed in this work was done with respect to the mass of iridium present on the RDE. Normalisation by geometric surface area of the RDE is not applicable for this purpose as it does not account for electrode loading effects. Normalisation by the electrocatalytically active surface area or the turn-over frequency is not feasible either for iridium-based OER catalysts, as it has been shown that on these materials the reaction is not a surface reaction but rather a sub-surface reaction with participation from oxide lattice oxygen species.[38–41] As normalisation metrics such as the turn-over frequency and the electrocatalytically active surface area account for only surface participation of the catalyst, these descriptors are not suitable as OER performance descriptors. Moreover, the determination, and even the definition, of an electrocatalytically active surface area of iridium oxides is problematic because of the contribution of bulk redox processes to the electrochemical response in the cyclic voltammograms of such oxides, which manifests in their supercapacitive behaviour.[42] Therefore, the most reasonable normalisation of the experimental current responses can at present only be done relative to the mass of iridium on the RDE,[37,43] as this offers the most technically relevant comparison of OER performance across different catalytic materials.

3. Results and discussion

3.1 Deposition yield

EDX analysis revealed an Ir mass loading of 9.4 ± 0.5 and 8.9 ± 0.3 wt% for two OMCD-batches of as-synthesised IrO_2/ATO catalyst. The synthesis procedure is shown to be reproducible in terms of the yield of Ir mass deposited, although the Ir loading achieved was significantly lower than the nominal target loading of 20 wt%. The reason for this loss of iridium during OMCD synthesis could be evaporation of the $Ir(acac)_3$ precursor: its vaporisation temperature at 190 °C[44,45] is below its decomposition temperature at 250 °C[45,46] in oxygen reactive gas. In literature, $Ir(acac)_3$ is reported as a suitable precursor for organometallic chemical vapour deposition where the precursor first needs to evaporate to form a vapour, after which it undergoes decomposition on the target substrate.[47]

However, in the presently used OMCD method, the vapour phase of the precursor is not required for the process, because the precursor is directly mixed with the support material. Instead, evaporation before decomposition of the precursor results in the transport of the precursor away from the support material, with subsequent deposition of iridium elsewhere, *e.g.* on the reactor walls. To minimise this iridium loss, we envisage optimisation of the reactor design as well as the exploration of alternative iridium precursors for this process.

3.2 Structural and chemical properties

X-ray diffraction (XRD) of IrO_2/ATO did not reveal any distinguishable features originating from metallic iridium or iridium oxide components, see Fig. S1 in ESI.† This is due to the similarity of the SnO_2 and IrO_2 rutile structure lattices, resulting in a masking of possible IrO_2 reflections by the corresponding SnO_2 reflections as a consequence of low Ir loading and small iridium oxide particle size (see HR-STEM results below).

This is consistent with previous observations,[32] where XRD did not detect Pt on ATO support even at metal loadings around 10 wt%, although crystalline Pt nanoparticles were clearly visible in HR-STEM. Hence, XRD is not a suitable technique to detect the presence and the phase of IrO_2 nanoparticles on ATO in the present study. However, the XRD pattern of OMCD IrO_2/ATO illustrates that the integrity of the ATO support is maintained during the deposition process, as the reflections are in the same positions as those seen in the XRD pattern of the bare ATO.

Fig. 2(a–f) shows representative HR-STEM images of the as-synthesised IrO_2/ATO catalyst, where it is seen that highly dispersed IrO_2 nanoparticles are present on the ATO support.

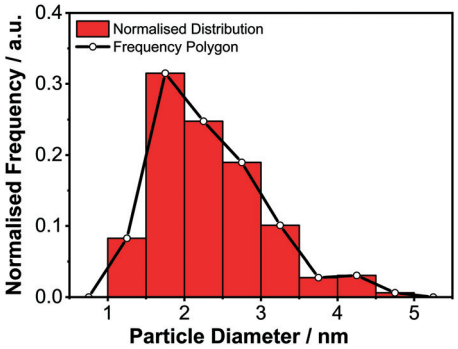

Fig. 3 Particle size distribution of IrO_2 nanoparticles over the ATO support.

The average IrO_2 particle diameter is 2.3 ± 0.7 nm (see particle size distribution in Fig. 3), which is comparable to sizes achieved using traditional wet chemistry deposition methods.[11,14,16,18,29] Careful analysis of the lattice spacings visible in the HR-STEM images (Fig. S4 in ESI†) confirmed the presence of rutile, tetragonal IrO_2 nanoparticles as listed in Table 1. However, some particles are indistinguishable, *i.e.* they can be either metallic Ir or rutile IrO_2 (particles 2, 4 and 6).

Furthermore, Fig. 2(c) and (f) show evidence of structural interactions between the deposited nanoparticles and the high surface area ATO support. The nanoparticle (higher HR-STEM contrast) that is also shown in Fig. 2(b) and (e) at lower magnification, has grown epitaxially, connecting to and extending the lattice planes of the rutile ATO support (lower HR-STEM contrast). Based on the lattice spacings of the particle alone, it was not possible to determine whether the nanoparticle is metallic iridium or rutile IrO_2 (particle 2 in Table 1). However, the epitaxial connection to the lattice

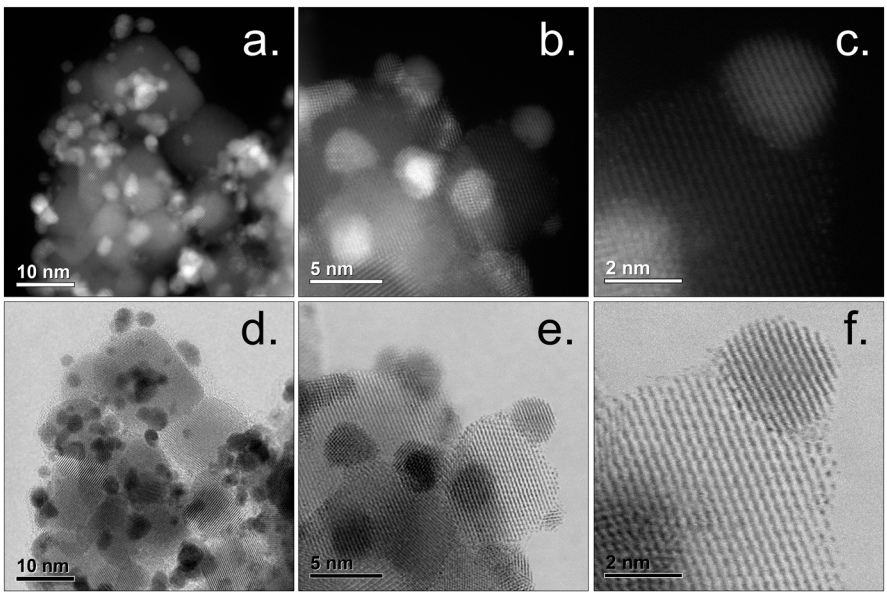

Fig. 2 High-resolution scanning transmission electron microscopy (HR-STEM) images of OMCD IrO_2/ATO (9 wt% Ir), where (a)–(c) are HAADF images and (d)–(f) are bright field images.

Table 1 Lattice spacings determined from HR-STEM images for 7 IrO_2 nanoparticles in OMCD IrO_2/ATO and comparison to the closest IrO_2 and Ir metal spacing (see Fig. S4† for HR-STEM images of these particles)

Particle	Measured *d*-spacing/Å	Closest *d*-spacing in tetragonal IrO_2/Å	Closest *d*-spacing in cubic Ir/Å	Most likely phase
1	2.42 ± 0.06	2.58 (101)	2.22 (111)	IrO_2
2	2.23 ± 0.02	2.25 (200)	2.22 (111)	Either Ir or IrO_2
3	2.41 ± 0.10	2.58 (101)	2.22 (111)	IrO_2
4	2.18 ± 0.04	2.25 (200)	2.22 (111)	Either Ir or IrO_2
5	2.26 ± 0.02	2.25 (200)	2.22 (111)	IrO_2
6	2.23 ± 0.12	2.25 (200)	2.22 (111)	Either Ir or IrO_2
7	2.58 ± 0.01	2.58 (101)	2.22 (111)	IrO_2

planes of the ATO support strongly suggests that this nanoparticle is indeed a rutile IrO_2 nanoparticle because of the matching rutile lattices of IrO_2 and SnO_2. The very slight tilting of the IrO_2 (200) planes with respect to the ATO (200) planes, in Fig. 2(f), could result from the IrO_2 (200) spacing (2.25 Å) being slightly smaller than the corresponding SnO2 (200) spacing (2.37 Å). In addition, the very similar HR-STEM-contrast of most visible IrO_2 nanoparticles is consistent with the presence of predominantly crystalline rutile iridium(IV) oxide nanoparticles produced by the OMCD process, with evidence of epitaxial anchoring on the high-surface-area ATO support.

EDX mapping provides further evidence on successful preparation of a supported catalyst, as shown in Fig. 4. The Sn signal is distributed uniformly across what we identify as the support material, while the Ir signal is clearly present in nanoparticles uniformly distributed across the ATO support.

XPS was performed to understand the chemical nature of the iridium species present in the as-prepared IrO_2/ATO catalyst, with results shown in Fig. 5. Analysis of the Ir 4f spectrum (Fig. 5(a)) proved that Ir^{4+} at 61.5 eV was the dominant Ir species, with a contribution of 74%. The remainder of the spectrum contains 22% Ir^{3+} at 62.4 eV and a small contribution from metallic iridium species (4%) at a binding energy of 60.8 eV. These results are in agreement with HR-STEM, where rutile iridium(IV) oxide was identified as the dominating phase from the OMCD process. While the OMCD deposition technique was successful in directly depositing crystalline IrO_2 nanoparticles on the ATO support in a one-step process, there is a small proportion of metallic iridium particles that did not undergo complete oxidation. In addition, the presence of Ir^{3+} in the Ir 4f XPS spectrum would suggest that the organometallic $Ir(acac)_3$ precursor did not fully decompose during the deposition process, while the presence of some Ir^{3+} containing oxyhydroxide species (IrO_x) cannot be excluded.

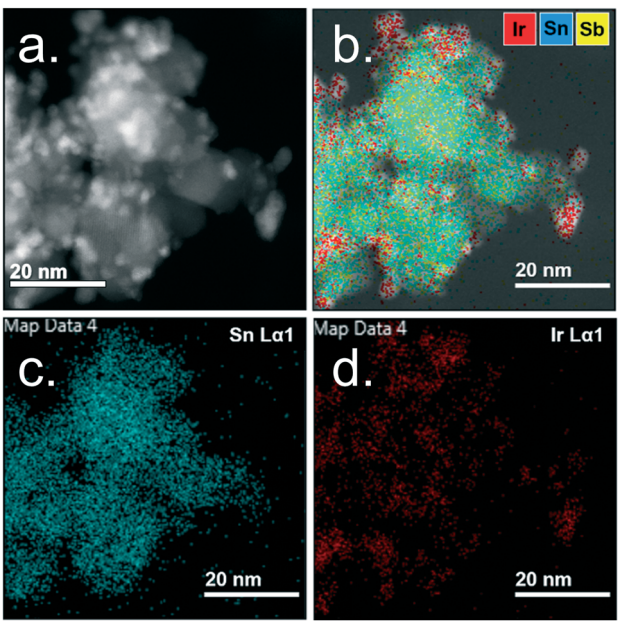

Fig. 4 HR-STEM EDX maps: (a) HAADF image for OMCD IrO_2/ATO, (b) colour composite elemental map (Ir, Sn and Sb) (c) Sn signal distribution and (d) Ir signal distribution.

From the O 1s spectrum (Fig. 5(b)), it can be concluded that the surface of the catalyst was hydrated. As the corresponding and most dominant peak at a binding energy of 531.5 eV presumably contains a contribution from both hydrated Ir and Sn oxides, it is not possible to distinguish between surface hydroxylation of the ATO support *versus* the iridium oxide. Peaks at higher binding energies are assigned to oxygen components arising from hydrocarbon species present at the surface of the catalyst. This is in agreement with the components detected from the C 1s signal: C–O at 286.3 eV and O–C=O at 288.8 eV, while aliphatic carbon was observed at 285.0 eV. The presence of hydrocarbon components is likely due to exposure to ambient air, as well as to incomplete hydrocarbon removal during $Ir(acac)_3$ decomposition, which potentially also acts as a surfactant and reducing agent for iridium-containing phases during the deposition process. In addition, the O 1s envelope contains a contribution from Sb $3d_{5/2}$ suggesting potential surface enrichment of this element. Given that photoelectrons are detected from the top ~5 nm of the sample surface, which is more than the average IrO_2 particle diameter, we consider the XPS results to represent compositional averages over both the surface and the bulk of the IrO_2 particles.

3.3 Electrochemical characterisation

The Ir mass-specific oxygen evolution activity of IrO_2/ATO was investigated in 0.1 M $HClO_4$ using chronoamperometric potential steps. Tafel plots of the Ir mass-specific OER currents before and after the stability test are shown in

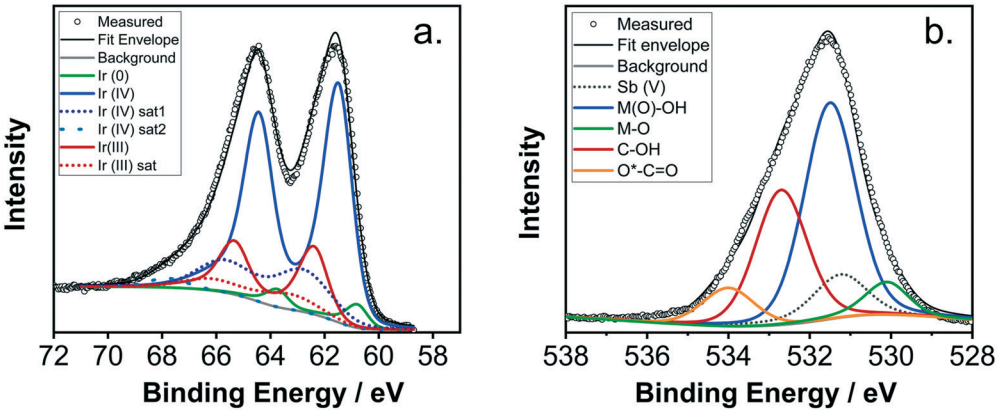

Fig. 5 (a) Ir 4f and (b) O 1s XPS spectra of OMCD IrO_2/ATO, where 'M' denotes the metals Sn, Sb and Ir.

Fig. 6(a). The Tafel slope for as-prepared OMCD IrO_2/ATO is 63 mV dec^{-1}, which is slightly higher than values usually reported for rutile IrO_2 catalysts[19,20,48,49] (between 50–60 mV dec^{-1}) as well as for the IrO_2–TiO_2 benchmark (54 mV dec^{-1}) obtained in this study. We attribute this to a limited electronic conductivity of our ATO support in combination with low Ir loading, which can result in an increased apparent Tafel slope as previously reported.[32,50] We note that lower Tafel slopes around 40 mV dec^{-1} have been reported for oxyhydroxide-type IrO_x catalysts,[6,35,51] where the degree of hydration has been shown to significantly lower the Tafel slope values compared to values reported for crystalline IrO_2. After stability evaluation, the Tafel slope of OMCD IrO_2/ATO was 58 mV dec^{-1}. This small decrease in Tafel slope is probably due to a small change in the degree of hydration during the stability tests.[51]

From extrapolation of the initial Tafel fit of the OMCD IrO_2/ATO, an Ir mass-specific activity of 10 A g_{Ir}^{-1} was obtained at a potential of 1.470 V *vs.* RHE (overpotential of 240 mV). For the IrO_2–TiO_2 benchmark catalyst, the same activity required a significantly higher potential of 1.524 V *vs.* RHE (overpotential of 294 mV). After stability evaluation, a similar trend was observed, where OMCD IrO_2/ATO required an overpotential of 256 mV to achieve a mass-specific activity of 10 A g_{Ir}^{-1}, whereas the commercial benchmark required an overpotential of 331 mV.

The OER electrocatalytic activity of OMCD IrO_2/ATO was evaluated for two separate OMCD-batches of the catalyst. EDX analysis revealed an Ir mass loading of 9.4 ± 0.5 and 8.9 ± 0.3 wt% for the two OMCD-batches of as-synthesised IrO_2/ATO catalyst, respectively. The reproducibility of the synthesis is clearly visible in Fig. 6(b); the Ir mass-specific oxygen evolution activity at 1.525 V *vs.* RHE was found to be 70 ± 7 A g_{Ir}^{-1} for the first batch, whereas the second batch achieved 73 ± 10 A g_{Ir}^{-1} at the same potential. These performances are 7 times higher than the activity of the IrO_2–TiO_2 commercial benchmark (10.4 ± 2 A g_{Ir}^{-1}), evaluated at similar Ir-based electrode loadings. Alternatively, for the same catalyst-based electrode loading, OMCD IrO_2/ATO achieved an OER mass-specific activity which was 13-fold greater than the commercial benchmark, when evaluated at 1.525 V *vs.* RHE, as seen in Fig. S3(b) in the ESI.†

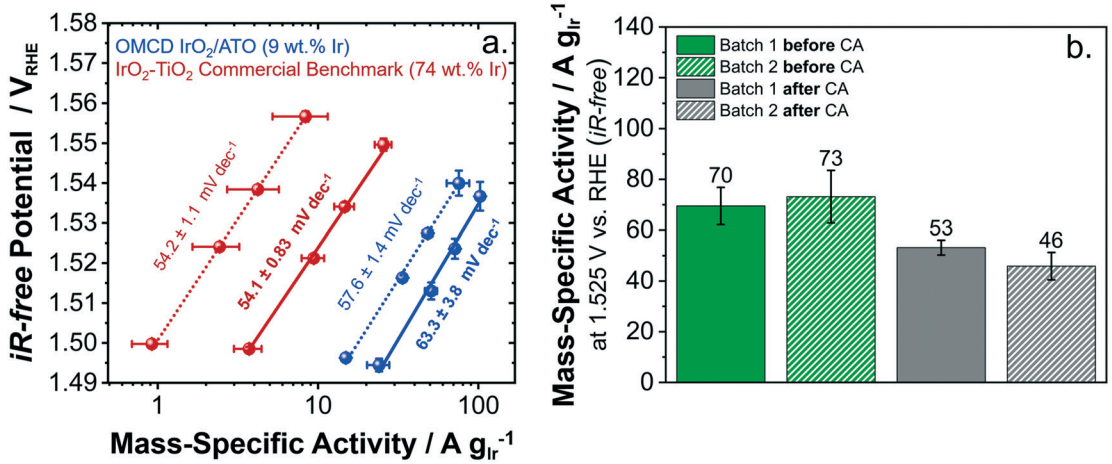

Fig. 6 (a) Mass-specific Tafel plots of OMCD IrO_2/ATO (average across two synthesis batches) and commercial IrO_2–TiO_2 benchmark before (solid lines) and after (dotted lines) stability experiments, where the commercial benchmark was evaluated at an electrode loading of 100 μg cm^{-2}. Electrolyte: 0.1 M $HClO_4$. (b) Mass-specific activity of two batches of OMCD IrO_2/ATO, before (green) and after (grey) stability tests.

After stability testing for 2 h at 1.600 V *vs.* RHE, the reproducibility of the OMCD method was further confirmed; batches 1 and 2 of OMCD IrO_2/ATO achieved mass-specific activities of 53 ± 3 and 46 ± 5 A g_{Ir}^{-1} at 1.525 V *vs.* RHE, respectively (Fig. 6(b)). On average, across the two catalyst batches, an overall relative loss of mass activity of ~31% was observed for OMCD IrO_2/ATO, *versus* 76% loss for the IrO_2–TiO_2 commercial benchmark when electrodes were prepared with similar Ir mass loadings. Nevertheless, the stability evaluation resulted in comparable mass-specific activity loss of 31% and 25% for OMCD IrO_2/ATO and IrO_2–TiO_2, respectively, when electrodes with the same catalyst loading were evaluated.

This is a promising outcome of the deposition method, as the more active IrO_2 nanoparticles of the OMCD IrO_2/ATO catalyst would be expected to be significantly less stable than the bulk-like IrO_2–TiO_2 benchmark. The epitaxial metal–support interactions observed in HR-STEM (Fig. 2) suggest that the strong stability of OMCD IrO_2/ATO is a consequence of the crystalline nature of the rutile IrO_2 nanoparticles in combination with a fortified structural anchoring on the ATO support. This is a direct outcome of the thermal nature of the OMCD process and the presence of the ATO during IrO_2 particle nucleation.

Post-catalysis HR-STEM characterisation was challenging to perform, as a result of Nafion® decomposition under the electron beam. Still, HR-STEM images of OMCD IrO_2/ATO after subjection to the electrochemical protocol reveal unchanged catalyst morphology (Fig. S5 of the ESI†).

As mentioned earlier, one of the drawbacks of wet synthesis methods is that in most cases the iridium or iridium oxide nanoparticles are synthesised separately and then added to the ATO support at later stages in the catalyst preparation process. This often results in much weaker metal–support interactions than in cases where the ATO support was present during the synthesis of the IrO_x nanoparticles.[52] Epitaxially grown nanoparticles have been found to have highly beneficial effects on the stability of supported catalysts for various reactions. For instance, Liu *et al.*[53] observed that epitaxial anchoring of Au nanoparticles supported on ZnO nanowires enhanced their resistance to catalyst deactivation by sintering, during CO oxidation. Similarly, the work by Li *et al.*[54] demonstrated that small nanoparticles (1–3 nm) of Rh, Pt and Ir were stabilised on $MgAl_2O_4$ particles by epitaxial anchoring, resulting in excellent thermal stability. Epitaxial metal–support interactions of RuO_2 coating films on SnO_2[55] and TiO_2[56] particles have also been reported. With relevance to the OER, RuO_2 overlayers epitaxially grown on PdO nanosheets[57] as well as IrO_x films on $SrIrO_3$[58] showed an improved electrocatalytic activity and stability compared to commercial OER catalyst nanoparticles, further demonstrating the benefits of structural epitaxial interactions at catalyst–support interfaces. From the perspective of our work, such epitaxial anchoring could lower the rate of deactivation mechanisms such as IrO_2 particle migration, agglomeration and detachment. Our OMCD IrO_2/ATO catalyst is one of the rare cases where epitaxial anchoring of electrocatalyst nanoparticles on high-surface area oxide support has been observed.

For unsupported iridium oxides, amorphous iridium oxyhydroxides, generally referred to as IrO_x, have been reported to be a factor of 16 times more active than crystalline rutile IrO_2.[34] On this basis, it is interesting to note that our OMCD catalyst was highly active towards OER, although both HR-STEM and XPS analyses showed that the dominating Ir phase in IrO_2/ATO was crystalline, rutile IrO_2. Unsupported rutile IrO_2 has a much lower active surface area than amorphous IrO_x.[34] Generally, small nanoparticles tend to have a higher quantity of exposed surface sites (edges, kinks, corners and steps), and a larger surface area to volume ratio per unit of mass; this results in higher catalytic activity than observed on bulk materials.[59] Dispersing such nanoparticles over suitable support materials can amplify these effects.[60] Therefore, a possible explanation for the outstanding OER activity combined with a high degree of crystallinity of the OMCD IrO_2/ATO is an enhancement of the electrocatalytically active surface area both due to the nanoparticulate geometry of rutile iridium(IV) oxide and due to its uniform dispersion over the ATO support. Additionally, the presence of some Ir^{3+}-containing oxyhydroxide and metallic iridium, indicated by XPS, may also contribute to the high mass-specific activity observed in OMCD IrO_2/ATO. The epitaxial anchoring of IrO_2 on ATO visible from HR-STEM (Fig. 2(c) and (f)) demonstrates the presence of a strong structural interaction of IrO_2 nanoparticles with the ATO support during nucleation and growth of the IrO_2 in the OMCD process, which explains their high degree of dispersion. Therefore, the OMCD method provides the right conditions to obtain a catalyst with optimal utilisation of crystalline IrO_2 for the OER.

Table 2 summarizes the information required to make comparisons between OMCD IrO_2/ATO and IrO_2 supported on ATO catalysts reported from other studies. A linear fit of the Tafel plot of ohmic-corrected Ir mass-specific OER activity was used to interpolate/extrapolate the activity to the potentials used in these other studies. We only consider literature data where the *ex situ* RDE method was used for OER catalyst characterization, and only cases where Ir-based nanoparticles have been deposited onto ATO. It should be noted that stability results have not been included in Table 2, owing to the variation of *ex situ* stability protocols in the OER community. Table 2 illustrates that the Ir mass-specific activity of OMCD IrO_2/ATO is at least on par with reported activities of a wide range of ATO-supported Ir-based electrocatalysts, with the exception of catalysts which were reported from four studies, one prepared by Adams' fusion,[20] one by microwave-assisted hydrothermal deposition[10] and two by polyol techniques.[28,29]

To discern the differences between the mass-activity achieved by OMCD IrO_2/ATO *versus* other works, it is necessary to understand that the performance of supported

Table 2 Comparison of catalytic performance of OMCD IrO_x/ATO to other studies on deposited Ir-based nanoparticles on ATO support

Ref.	Deposition method	IrO_x nanoparticle size/nm	Dominant Ir phase(s) present in 'as-prepared' material	Iridium loading/wt%	Tafel slope/mV dec^{-1}	Mass-specific OER activity/A g_{Ir}^{-1} Potential/V_{RHE} (iR-free)	Ref.	This work
This work	***OMCD***	***1–5***	***Rutile IrO_2***	***9***	***63***	***1.525***	—	***70***
20	Adams' fusion	5–8	Rutile IrO_2	43[d]	54	1.550[a,b]	240[c]	***184***
16	Polyol	1.0–4.5	Ir metal	17	57–59	1.510	39	***43***
10	Microwave-assisted hydrothermal	2–4	Oxyhydroxide IrO_x	33[e]	NA[f]	1.580	1300	***550***
19	Colloidal	3–6	Rutile IrO_2	26[d]	51	1.600	467[c]	***1040***
18	Chemical reduction	0.5–3.5	Ir metal with oxyhydroxide IrO_x shell	29	NA	1.510	38	***43***
11	Solvothermal	2–3	Rutile IrO_2	25	NA	1.530	63	***89***
29	Polyol	0.5–3.0	Ir metal with oxyhydroxide IrO_x shell	11	45	1.500	185	***31***
27	Hydrothermal	1–2	Oxyhydroxide IrO_x	22	NA	1.550	41.3	***184***
	Hydrothermal + calcination	20–30	Rutile IrO_2	24	NA	1.600	2.7	***1040***
28	Polyol	*ca.* 1.4 nm	Oxyhydroxide IrO_x	17	50	1.510	250	***43***

[a] Potential converted from the reported *vs.* saturated calomel electrode (SCE) to *vs.* RHE assuming 0.0 V_{SCE} = 0.300 V_{RHE}. [b] Potential not reported as iR-free in literature work. [c] Ir mass-specific activity calculated from a different reported activity metric. [d] Ir loading calculated from reported IrO_2 loading. [e] Ir loading in mol%. [f] Not applicable.

iridium-based OER catalysts is a function of various physical properties, the spatial distribution of the deposited nanoparticles over the support, the crystallinity and particle size of the deposited iridium phases, the oxidation state of the iridium, the physical properties of the ATO support (conductivity and surface area), and lastly the presence of metal–support interactions.

For instance, Tong *et al.*[19] prepared IrO_2 particles with sizes which ranged from 3–6 nm, whereas in our work smaller particle sizes of 1–5 nm were deposited. Therefore, our approximately 2.2 times higher mass-activity observed at 1.600 V *vs.* RHE can possibly be attributed to OMCD IrO_2/ATO having a higher surface area, as a result of smaller IrO_2 particles. OMCD IrO_2/ATO demonstrated comparable mass-specific activity to a catalyst where IrO_2 nanoparticles were deposited onto macroporous ATO using a solvothermal method.[11] This is in agreement with the comparable particle size and dominating presence of the IrO_2 phase. The most recent work by da Silva *et al.*[27] involved the deposition of both hydrous IrO_x and crystalline IrO_2 onto ATO support, using a hydrothermal method. The hydrous IrO_x/ATO catalyst exhibited a 5-times lower mass-specific activity than OMCD IrO_2/ATO at a potential of 1.550 V *vs.* RHE, whereas at a potential of 1.600 V *vs.* RHE, the crystalline IrO_2/ATO in da Silva *et al.*[27] had an activity of ~3 A g_{Ir}^{-1}, which is very low compared to the activity of our crystalline IrO_2/ATO from OMCD. Our promising result further illustrates the potential of the OMCD IrO_2/ATO catalyst, combining the good stability of the highly crystalline IrO_2 nanoparticles with the OER performance of some hydrous IrO_x catalysts, although the latter are generally expected to be much more active. On the contrary, Liu *et al.*[20] prepared rutile IrO_2 nanoparticles on ATO nanowires; reporting a slightly higher mass-specific OER activity in comparison to our work at 1.55 V *vs.* RHE, despite their larger IrO_2 nanoparticle sizes of 5–8 nm. This relatively small difference in activity compared to the OMCD IrO_2/ATO may be attributed to the nanowire morphology of the ATO support.

The nature of the Ir-phases present, for the reported ATO supported Ir-based electrocatalysts, must be also considered. It is known that metallic iridium becomes electrochemically activated and converted to hydrous, amorphous iridium oxides during the application of an oxidising potential.[41,61] These species have been shown to exhibit much higher OER activity than thermally prepared iridium oxides, due to higher surface area and nature of the Ir species.[34] This relation can be used for comparisons between OMCD IrO_2/ATO *versus* instances where metallic Ir and oxyhydroxides were deposited onto various ATO supports.[10,16,18,27,28] Firstly, the mass-activity of OMCD IrO_2/ATO was comparable to these studies.[16,18] However, approximately 2 to 6 times larger Ir mass-specific activities reported by Massué *et al.*,[10] Hartig-Weiss *et al.*[29] and Abbou *et al.*,[28] respectively, can be directly related to the dominating presence of electrochemically formed iridium oxides in these studies. Furthermore, these studies were conducted on ATO supports synthesized for optimised surface area and electronic conductivity that may contribute towards the higher mass-activity values reported. This suggests that the performance of OMCD IrO_2/ATO can be further improved by optimisation of the ATO support, on the basis of its electronic conductivity and surface area.

4. Conclusions

We have demonstrated a simple and reproducible method for the deposition of crystalline iridium(IV) dioxide nanoparticles

on ATO, in a one-step, organometallic chemical deposition (OMCD) process. The rutile crystalline nature of the IrO_2 nanoparticles, their uniform dispersion across the ATO surface, and their predominant Ir(IV) oxidation state were confirmed by HR-STEM and XPS analysis, respectively. Most interestingly, HR-STEM provided evidence for the presence of epitaxial anchoring of IrO_2 nanoparticles deposited on the ATO support. These physicochemical properties of the OMCD IrO_2/ATO translated into an intriguing OER performance: the IrO_2 nanoparticulate geometry and uniform distribution resulted in high iridium utilisation and an outstanding Ir mass-specific OER activity that was superior to a commercially available crystalline IrO_2–TiO_2 benchmark. Remarkably, the performance of our crystalline IrO_2/ATO was competitive with OER activities reported from other studies for ATO-supported iridium-based catalysts that comprised highly active hydrous-amorphous IrO_x phases. Thus, OMCD has proven to be a facile and robust method to deposit crystalline IrO_2 nanoparticles that are observed to epitaxially interact with the ATO support, resulting in competitive OER activity in combination with the robust stability of crystalline IrO_2 strongly anchored on the support. As a route to further improve the OMCD process, we envisage the implementation of an improved OMCD reactor design and exploration of alternative iridium precursors to minimise iridium losses during the deposition process, and to demonstrate its scalability.

Conflicts of interest

There are no conflicts to declare.

Acknowledgements

The work was financially supported by the South African Department of Science and Innovation in the form of HySA/Catalysis Centre of Competence programme funding. Z. S. H. S. R. acknowledges the Dutkiewicz Family Scholarship for postgraduate energy research. This work is based on the research supported in part by the National Research Foundation of South Africa Grant numbers 93205 and 94878. B. P. Doyle and E. Carleschi are acknowledged for the XPS measurements. R. Martin is acknowledged for assistance with HR-STEM imaging analysis, as well as for many fruitful scientific discussions. The Centre for High Resolution Transmission Electron Microscopy at Nelson Mandela Metropolitan University in Port Elizabeth is graciously acknowledged for use of their JEOL JEM ARM200F electron microscope. The electron microscopy unit at the University of Cape Town, and in particular N. Hanief and M. Waldron, are acknowledged for their assistance with EDX measurements.

References

1 T. Reier, M. Oezaslan and P. Strasser, *ACS Catal.*, 2012, **2**, 1765–1772.
2 Y. T. Kim, P. P. Lopes, S. A. Park, A. Y. Lee, J. Lim, H. Lee, S. Back, Y. Jung, N. Danilovic, V. Stamenkovic, J. Erlebacher, J. Snyder and N. M. Markovic, *Nat. Commun.*, 2017, **8**, 1–8.
3 H. N. Nong, L. Gan, E. Willinger, D. Teschner and P. Strasser, *Chem. Sci.*, 2014, **5**, 2955–2963.
4 L. E. Owe, M. Tsypkin, K. S. Wallwork, R. G. Haverkamp and S. Sunde, *Electrochim. Acta*, 2012, **70**, 158–164.
5 T. Audichon, E. Mayousse, S. Morisset, C. Morais, C. Comminges, T. W. Napporn and K. B. Kokoh, *Int. J. Hydrogen Energy*, 2014, **39**, 16785–16796.
6 D. F. Abbott, D. Lebedev, K. Waltar, M. Povia, M. Nachtegaal, E. Fabbri, C. Copéret and T. J. Schmidt, *Chem. Mater.*, 2016, **28**, 6591–6604.
7 R. D. L. Smith, B. Sporinova, R. D. Fagan, S. Trudel and C. P. Berlinguette, *Chem. Mater.*, 2014, **26**, 1654–1659.
8 A. T. Marshall and R. G. Haverkamp, *Electrochim. Acta*, 2010, **55**, 1978–1984.
9 R. E. Fuentes, J. Farell and J. W. Weidner, *Electrochem. Solid-State Lett.*, 2011, **14**, 62–64.
10 C. Massué, V. Pfeifer, X. Huang, J. Noack, A. Tarasov, S. Cap and R. Schlögl, *ChemSusChem*, 2017, **10**, 1943–1957.
11 D. Böhm, M. Beetz, M. Schuster, K. Peters, A. G. Hufnagel, M. Döblinger, B. Böller, T. Bein and D. Fattakhova-Rohlfing, *Adv. Funct. Mater.*, 2019, 1906670.
12 D. Lebedev and C. Copéret, *ACS Appl. Energy Mater.*, 2019, **2**, 196–200.
13 W. Hu, S. Chen and Q. Xia, *Int. J. Hydrogen Energy*, 2014, **39**, 6967–6976.
14 V. K. Puthiyapura, M. Mamlouk, S. Pasupathi, B. G. Pollet and K. Scott, *J. Power Sources*, 2014, **269**, 451–460.
15 H. S. Oh, H. N. Nong, T. Reier, M. Gliech and P. Strasser, *Chem. Sci.*, 2015, **6**, 3321–3328.
16 H. S. Oh, H. N. Nong, T. Reier, A. Bergmann, M. Gliech, J. Ferreira De Araújo, E. Willinger, R. Schlögl, D. Teschner and P. Strasser, *J. Am. Chem. Soc.*, 2016, **138**, 12552–12563.
17 H. Ohno, S. Nohara, K. Kakinuma, M. Uchida and H. Uchida, *Catalysts*, 2019, **9**, 5–7.
18 L. Solà-Hernández, F. Claudel, F. Maillard and C. Beauger, *Int. J. Hydrogen Energy*, 2019, **44**, 24331–24341.
19 J. Tong, Y. Liu, Q. Peng, W. Hu and Q. Wu, *J. Mater. Sci.*, 2017, **52**, 13427–13443.
20 G. Liu, J. Xu, Y. Wang and X. Wang, *J. Mater. Chem. A*, 2015, **3**, 20791–20800.
21 C. Rozain, E. Mayousse, N. Guillet and P. Millet, *Appl. Catal., B*, 2016, **182**, 153–160.
22 F. Maillard, A. Bonnefont and F. Micoud, *Electrochem. Commun.*, 2011, **13**, 1109–1111.
23 K. Sasaki, F. Takasaki, Z. Noda, S. Hayashi, Y. Shiratori and K. Ito, *ECS Trans.*, 2010, **33**, 473–482.
24 E. Elangovan and K. Ramamurthi, *Appl. Surf. Sci.*, 2005, **249**, 183–196.
25 T. Nütz, U. Zum Felde and M. Haase, *J. Chem. Phys.*, 1999, **110**, 12142–12150.
26 J. Zhang and L. Gao, *Mater. Res. Bull.*, 2004, **39**, 2249–2255.

27 G. C. da Silva, S. I. Venturini, S. Zhang, M. Löffler, C. Scheu, K. J. J. Mayrhofer, E. A. Ticianelli and S. Cherevko, *ChemElectroChem*, 2020, **7**, 2330.
28 S. Abbou, R. Chattot, V. Martin, F. Claudel, L. Solá-Hernandez, C. Beauger, L. Dubau and F. Maillard, *ACS Catal.*, 2020, DOI: 10.1021/acscatal.0c01084, Just Accepted Manuscript.
29 A. Hartig-Weiss, M. Miller, H. Beyer, A. Schmitt, A. Siebel, A. T. S. Freiberg, H. A. Gasteiger and H. A. El-Sayed, *ACS Appl. Nano Mater.*, 2020, **3**, 2185–2196.
30 C. Jackson, O. Conrad and P. Levecque, *Electrocatalysis*, 2017, **8**, 224–234.
31 S. Taylor, E. Fabbri, P. Levecque, T. J. Schmidt and O. Conrad, *Electrocatalysis*, 2016, **7**, 287–296.
32 R. Mohamed, T. Binninger, P. J. Kooyman, A. Hoell, E. Fabbri, A. Patru, A. Heinritz, T. J. Schmidt and P. Levecque, *Catal. Sci. Technol.*, 2018, **8**, 2672–2685.
33 V. A. Saveleva, L. Wang, O. Kasian, M. Batuk, J. Hadermann, J. J. Gallet, F. Bournel, N. Alonso-Vante, G. Ozouf, C. Beauger, K. J. J. Mayrhofer, S. Cherevko, A. S. Gago, K. A. Friedrich, S. Zafeiratos and E. R. Savinova, *ACS Catal.*, 2020, **10**, 2508–2516.
34 V. Pfeifer, T. E. Jones, J. J. V. Vélez, C. Massué, R. Arrigo, D. Teschner, F. Girgsdies, M. Scherzer, M. T. Greiner, J. Allan, M. Hashagen, G. Weinberg, S. Piccinin, M. Hävecker, A. Knop-Gericke and R. Schlögl, *Surf. Interface Anal.*, 2016, **48**, 261–273.
35 H. Yu, N. Danilovic, Y. Wang, W. Willis, A. Poozhikunnath, L. Bonville, C. Capuano, K. Ayers and R. Maric, *Appl. Catal., B*, 2018, **239**, 133–146.
36 A. C. Garcia and M. T. M. M. Koper, *ACS Catal.*, 2018, **8**, 9359–9363.
37 E. Fabbri, A. Habereder, K. Waltar, R. Kötz and T. J. Schmidt, *Catal. Sci. Technol.*, 2014, **4**, 3800–3821.
38 T. Binninger, R. Mohamed, K. Waltar, E. Fabbri, P. Levecque, R. Kötz and T. J. Schmidt, *Sci. Rep.*, 2015, **5**, 1–7.
39 V. Pfeifer, T. E. Jones, S. Wrabetz, C. Massué, J. J. Velasco Vélez, R. Arrigo, M. Scherzer, S. Piccinin, M. Hävecker, A. Knop-Gericke and R. Schlögl, *Chem. Sci.*, 2016, **7**, 6791–6795.
40 A. Grimaud, O. Diaz-Morales, B. Han, W. T. Hong, Y. L. Lee, L. Giordano, K. A. Stoerzinger, M. T. M. Koper and Y. Shao-Horn, *Nat. Chem.*, 2017, **9**, 457–465.
41 V. A. Saveleva, L. Wang, D. Teschner, T. Jones, A. S. Gago, K. A. Friedrich, S. Zafeiratos, R. Schlögl and E. R. Savinova, *J. Phys. Chem. Lett.*, 2018, **9**, 3154–3160.
42 B. E. Conway, *Electrochemical supercapacitors: scientific fundamentals and technological applications*, Plenum Press, 1999.
43 C. Wei, R. R. Rao, J. Peng, B. Huang, I. E. L. L. Stephens, M. Risch, Z. J. Xu and Y. Shao-Horn, *Adv. Mater.*, 2019, **1806296**, 1–24.
44 Y. M. Sun, J. P. Endle, K. Smith, S. Whaley, R. Mahaffy, J. G. Ekerdt, J. M. White and R. L. Hance, *Thin Solid Films*, 1999, **346**, 100–107.
45 J. R. Vargas Garcia, T. Goto, J. R. V. Garcia and T. Goto, *Mater. Trans.*, 2003, **44**, 1717–1728.
46 I. Igumenov, *J. Phys. IV*, 1995, **05**, C5-489-C5-496.
47 V. Y. Vasilyev, N. B. Morozova, T. V. Basova, I. K. Igumenov and A. Hassan, *RSC Adv.*, 2015, **5**, 32034–32063.
48 M. E. G. Lyons and S. Floquet, *Phys. Chem. Chem. Phys.*, 2011, **13**, 5314–5335.
49 E. Antolini, *ACS Catal.*, 2014, **4**, 1426–1440.
50 C. P. De Pauli and S. Trasatti, *J. Electroanal. Chem.*, 2002, **538**, 145–151.
51 A. Minguzzi, C. Locatelli, O. Lugaresi, E. Achilli, G. Cappelletti, M. Scavini, M. Coduri, P. Masala, B. Sacchi, A. Vertova, P. Ghigna and S. Rondinini, *ACS Catal.*, 2015, **5**, 5104–5115.
52 C. Spöri, J. T. H. Kwan, A. Bonakdarpour, D. P. Wilkinson and P. Strasser, *Angew. Chem., Int. Ed.*, 2017, **56**, 5994–6021.
53 J. Liu, B. Qiao, Y. Song and J. Jimmy, *Chem. Commun.*, 2015, **51**, 15332–15335.
54 W. Z. Li, L. Kovarik, D. Mei, M. H. Engelhard, F. Gao, J. Liu, Y. Wang and C. H. F. Peden, *Chem. Mater.*, 2014, **26**, 5475–5481.
55 D. Teschner, R. Farra, L. Yao, R. Schlögl, H. Soerijanto, R. Schomäcker, T. Schmidt, L. Szentmiklósi, A. P. Amrute, C. Mondelli, J. Pérez-Ramírez, G. Novell-Leruth and N. López, *J. Catal.*, 2012, **285**, 273–284.
56 A. Kim, C. Sanchez, G. Patriarche, O. Ersen, S. Moldovan, A. Wisnet, C. Sassoye and D. P. Debecker, *Catal. Sci. Technol.*, 2016, **6**, 8117–8128.
57 Y. Hu, X. Luo, G. Wu, T. Chao, Z. Li, Y. Qu, H. Li, Y. Wu, B. Jiang and X. Hong, *ACS Appl. Mater. Interfaces*, 2019, **11**, 42298–42304.
58 L. C. Seitz, C. F. Dickens, K. Nishio, Y. Hikita, J. Montoya, A. Doyle, C. Kirk, A. Vojvodic, H. Y. Hwang, J. K. Norskov and T. F. Jaramillo, *Science*, 2016, **353**, 1011–1014.
59 P. Munnik, P. E. De Jongh and K. P. De Jong, *Chem. Rev.*, 2015, **115**, 6687–6718.
60 R. A. van Santen, *Acc. Chem. Res.*, 2009, **42**, 57–66.
61 R. Kötz, H. Neff and S. Stucki, *J. Electrochem. Soc.*, 1984, **131**, 72.

